

Uncertainties of the 30-408 MHz Galactic emission as a calibration source for radio detectors in astroparticle physics

M. Büsken^{1,2}, T. Fodran³, and T. Huege^{4,5}

¹ Institute for Experimental Particle Physics, Karlsruhe Institute of Technology, Hermann-von-Helmholtz-Platz 1, 76344 Eggenstein-Leopoldshafen, Germany

² Instituto de Tecnologías en Detección y Astropartículas, Universidad, Universidad Nacional de San Martín, Av. General Paz 1555 (B1630KNA), San Martín, Buenos Aires, Argentina
e-mail: max.buesken@kit.edu

³ Department of Astrophysics/IMAPP, Radboud University, P.O. Box 9010, 6500 GL Nijmegen, The Netherlands
e-mail: t.fodran@science.ru.nl

⁴ Institute for Astroparticle Physics, Karlsruhe Institute of Technology, Hermann-von-Helmholtz-Platz 1, 76344 Eggenstein-Leopoldshafen, Germany

⁵ Physics Department, Vrije Universiteit Brussels, Pleinlaan 2, 1050 Brussels, Belgium
e-mail: tim.huege@kit.edu

Received / Accepted

ABSTRACT

Context. Arrays of radio antennas have proven to be successful in astroparticle physics with the observation of extensive air showers initiated by high-energy cosmic rays in the Earth's atmosphere. Accurate determination of the energy scale of the primary particles' energies requires an absolute calibration of the radio antennas for which, in recent years, the utilization of the Galactic emission as a reference source has emerged as a potential standard.

Aims. To apply the "Galactic Calibration", a proper estimation of the systematic uncertainties on the prediction of the Galactic emission from sky models is necessary, which we aim to determine on a global level as well as for the specific cases of selected radio arrays. We further aim to quantify the influence of the quiet Sun on the Galactic Calibration.

Methods. We look at four different sky models that predict the full-sky Galactic emission in the frequency range from 30 to 408 MHz and compare them. We make an inventory of the reference maps on which they rely and use the output of the models to determine their global level of agreement. Next, we take the sky exposures and frequency bands of selected radio arrays into account and repeat the comparison for each of them. Finally, we study the relative influence of the Sun in its quiet state by projecting it onto the sky with brightness data from recent measurements.

Results. We find systematic uncertainty of 12 % on the predicted power from the Galactic emission, which scales to approximately half of that value as the uncertainty on the determination of the energy of cosmic particles. When looking at the selected radio arrays, the uncertainty on the predicted power varies between 10 % and 19 %. The influence of the quiet Sun turns out to be insignificant at the lowest frequencies but increases to a relative contribution of $\sim 20\%$ around 400 MHz.

Key words. Astroparticle physics – Methods: miscellaneous – Radio continuum: general – Sun: radio radiation

1. Introduction

Already in the 1940s, surveys of the sky at radio frequencies were conducted. Strong emission from the constellation of Sagittarius was found as well as smaller maxima originating in extragalactic sources (e.g. Cygnus A, Cassiopeia A) and at this point also a signal coming from the Sun was seen (Reber 1944). In measurement campaigns, the entire sky was mapped at specific frequencies. These maps show strong point-like sources as well as the diffuse radio emission from the Galaxy. The original motivation for this was to get a better understanding of the Galaxy and also to use the information from the maps in studies in the fields of astronomy and astrophysics, e.g. related to the cosmic microwave background. To acquire accurate descriptions of the Galactic emission not only from a handful of maps at some specific frequencies but across a broad frequency range for the whole sky, efforts were made to build models of the radio sky based on these reference maps.

These sky models recently became relevant in the field of astroparticle physics for the absolute calibration of radio detection arrays. Over the past years, the radio detection technique has gained increasing importance for the observation of highly energetic cosmic rays and neutrinos detected through the radio emission from particle cascades (Huege 2016; Schröder 2017). A number of promising radio detection arrays for the measurement of cosmic particles in the frequency range from a few tens to hundreds of MHz are in the phase of development or under construction (e.g. the AugerPrime Radio Detector (Pont 2019), the Square Kilometer Array low-frequency site (SKA-low) (Buitink et al. 2021), the Giant Radio Array for Neutrino Detection (GRAND) (Álvarez-Muñiz et al. 2020)) while some are already taking data (e.g. the Auger Engineering Radio Array (AERA) (Huege, T., Aab, A., Abreu, P., et al. 2019), the LOw Frequency ARray (LOFAR) (Schellart, P. et al. 2013)). For extracting physics it is very important to accurately determine the absolute energy scale of the detected particle cascades – and therefore an accurate calibration of the radio detectors is

required. Calibrating with a reference antenna emitting a defined signal (e.g. mounted on a drone (Aab et al. 2017)) has the disadvantage of uncertainties on the emitted signal strength which are difficult to assess (Mulrey et al. 2019). Also, dedicated calibration campaigns require significant effort and are almost impossible to perform on a regular basis for large arrays. A different calibration approach uses the diffuse Galactic radio emission – which poses a natural background to the detection of radio emission from particle showers – as the reference signal. It typically poses the dominant background from natural sources at these frequencies (Union 2019). This so-called Galactic Calibration also offers the opportunity to directly compare the calibration of different radio arrays as they at least partially see the same sky. Moreover, the method can be applied as regularly as background data is available and does not require special field campaigns. The Galactic Calibration was already applied to the LOFAR low-band antennas (Mulrey et al. 2019) and to the engineering array of the new radio detector of the Pierre Auger Observatory (Fodran et al. 2021).

In the Galactic Calibration, the measured background signal from the Galaxy is compared to predictions made with the aforementioned sky models. Knowing the uncertainty on these predictions is thus crucial for a useful absolute calibration. In this work, we therefore conduct a comparison of four publicly available radio sky interpolation models for the frequency range from 30 to 408 MHz. We do this by generating outputs with the models, calculating the average sky temperature from the outputs and determining the level of agreement between the models. From this comparison we get an estimate for the systematic uncertainties of the modeled background predictions for the Galactic Calibration.

First we present these models (Sect. 2) and summarize the reference maps they are based on (Sect. 3). Afterwards, we perform a global comparison while also showing other, less detailed descriptions of the radio background (Sect. 4). After that we adjust the comparison for the sky seen by an observer at a specific location on Earth. We further conduct the comparison tailored to a set of selected radio arrays from the present and future, namely the Radio Neutrino Observatory Greenland (RNO-G) (Aguilar et al. 2021), LOFAR (Schellart, P. et al. 2013), GRAND (Álvarez-Muñiz et al. 2020), SKA-low (Buitink et al. 2021), the radio detectors of the Pierre Auger Observatory (Huege, T., Aab, A., Abreu, P., et al. 2019; Pont 2019) and IceCube (Abbasi et al. 2021). Additionally, we study the influence of the quiet Sun as another source in the radio sky on the background (Sect. 6). Finally, we discuss implications of the results for the application of the Galactic Calibration (Sect. 7) to radio detectors in astroparticle physics.

2. Radio sky interpolation models

In the past years, a couple of models for predicting the diffuse foreground emission of the sky in the radio and microwave regimes were developed with the purpose of calibrating radio arrays or removing this foreground emission from measurements of the cosmic microwave background.

These models interpolate between reference sky surveys at various frequencies conducted with telescopes at different locations. In the surveys, the sky brightness at given coordinates is mapped in terms of the brightness temperature T_B . This is the temperature of a thermal radiator, i.e. a black body, that would show the same brightness as the one measured. In the classical limit $h\nu \ll k_B T$ of Planck's law for black body radiation, where h is the Planck constant, ν is the considered frequency and k_B

is the Boltzmann constant, the Rayleigh-Jeans law is applicable. The brightness temperature is then directly proportional to the observed brightness I_ν [$\text{Wm}^{-2}\text{Hz}^{-1}\text{sr}^{-1}$]: (Wilson et al. 2009)

$$T_B = \frac{c^2}{2k_B \cdot \nu^2} I_\nu, \quad (1)$$

where c is the speed of light in vacuum. In the frequency range from a few 10 MHz to a few 100 MHz, most of the electromagnetic background in the sky is presumably synchrotron radiation from electrons gyrating in the magnetic field of the Galaxy (Rybicki & Lightman 1985). Although this is non-thermal emission, the description of the radio sky by a brightness temperature is still practical because of its proportionality to the brightness I_ν .

The frequency dependence of the brightness temperature can be described at lower radio frequencies by a power-law

$$T_B \propto \nu^\beta \quad (2)$$

with a spectral index β . Recent studies of the spectral index at frequencies from 50 MHz to 200 MHz lie in a range of $-2.62 < \beta < -2.46$, depending on the region in the sky (Mozdzen et al. 2016, 2018; Rogers & Bowman 2008). Around 200 MHz and again above 400 MHz, changes of the spectral index are observed with a steepening towards higher frequencies (Purton 1966; Bridle & Baldwin 1967; Webster 1974).

This relation can be used to scale a single full-sky reference map from a survey conducted at a low frequency to any other frequency. One model, called LFmap, uses this approach of spectral scaling with frequency- and region-specific spectral indices for interpolation. LFmap is included in the model comparison of this work. Other popular interpolation models use the approach of a principal component analysis (PCA) of multiple reference maps to produce frequency-dependent descriptions of the radio sky. In this inventory, three such models will be considered and introduced in the following Sects. namely the Global Sky Model (GSM) in its first (de Oliveira-Costa et al. 2008) and improved (Zheng et al. 2016) version, as well as the Low Frequency Sky Model (LFSM) (Dowell et al. 2017).

2.1. LFmap

The LFmap (Polisensky 2007) software is a radio sky interpolation software based on the simple power-law model for the sky brightness temperature (Eq. 2). The 408 MHz map by Haslam et al. (1982) in the revisited version by Platania et al. (2003) is scaled down with spectral indices from a spectral index map from the same reference to frequencies down to a minimum frequency of 180 MHz. To take spectral bending into account, new spectral indices are used for frequencies below 180 MHz, which are calculated such that each pixel of the downscaled map at 180 MHz scales onto the same pixel of a 22 MHz map by Roger, R. S. et al. (1999). Part of the region around the Galactic center is affected by HII absorption, which becomes relevant only below 45 MHz. Therefore, an intermediate step at this frequency is introduced, where the affected region of the map is replaced by the average of the surrounding area, that is unaffected by HII absorption. Below 45 MHz the procedure of calculating spectral indices is done with the original 22 MHz map. In a similar manner, regions not covered in the 22 MHz map are replaced with averages from surrounding areas. Most point-like sources are not treated individually, except for the two brightest ones, for which adapted

spectral indices are used to scale their brightness temperatures. In this study, we use the default settings of LFmap.

2.2. GSM (2008)

The other three considered radio sky interpolation models use a principal component analysis (PCA) to generate all-sky maps at any intermediate frequency. Of these models, GSM (de Oliveira-Costa et al. 2008) is the oldest, which uses the fewest reference maps. The advantage of a PCA is that also maps of limited sky coverage can be used. However, different angular resolutions and levels of quality between the used maps pose challenges for this approach. In GSM, also maps at GHz frequencies are used, which can have a significant influence on the low-frequency results in regions where there is otherwise only sparse map coverage.

The PCA in GSM is performed for the region of the sky that is covered by all of the included reference maps. In a fit, the principal components are modeled to best match in the remaining regions. At minimum, there is information from six maps per pixel. However, for a large part of the southern hemisphere, sub-GHz information is only available from the all-sky maps at 45 MHz and 408 MHz, possibly reducing the model accuracy in this region at these frequencies, which is relevant for experiments located in the southern hemisphere. The resulting sky description with principal components at the reference frequencies is finally spline-interpolated to any frequency in between. No special treatment for point-like sources is mentioned although they were removed in some of the used reference maps.

The accuracy of the model is determined by taking one of the reference maps out of the calculation of the principal components and calculating the difference of this map to the output of the model at that frequency without the information from the map. This is done for all frequencies at which a reference map is available and gives an estimate for the accuracy of around 12 % for the sub-GHz maps. However, the model does not account for individual uncertainties associated with the reference maps or systematic temperature shifts of a map over the whole sky, that could be introduced by inaccurate calibration.

2.3. GSM (2016)

The original GSM received an update in which further reference maps were included and the model algorithm around the PCA was improved (Zheng et al. 2016). The frequency range of the model was extended to 5 THz by including recently published surveys in the microwave regime. At lower radio frequencies, maps at 85 MHz and 150 MHz were added. With this enhanced set of surveys, there is no common region covered by all of them, that can be used for conducting the PCA as in the original GSM. Instead, an iterative algorithm is implemented, which fits the principal components to the reference maps to the desired accuracy. For the zeroth iteration, a subset of maps was used that overlap by at least 5 % in sky coverage. Then the remaining maps were fed into the model. Finally, six principal components are used, compared to three components in the original GSM. Within the PCA algorithm, point-like sources are removed.

A level of model accuracy is determined in the same way as for the original GSM and found to be around 8 % for the sub-GHz frequencies. When compared to the original GSM, the accuracy of the improved model is better for all sub-GHz frequencies by a factor of up to 2. However, since the original GSM is still widely used and since most of the newly added reference

maps are at higher frequencies than we consider here, we include both versions of the GSM in the comparison of this study.

2.4. LFSM

Based on the sky surveys at the Long Wavelength Array Station 1 (LWA1) (Ellingson et al. 2013) in the USA at frequencies from 40 MHz to 80 MHz, a low-frequency sky model was constructed (Dowell et al. 2017). Additional surveys from the literature were included. The model itself is based on the PCA approach as performed in the original GSM. Similar to the improved GSM, an iterative procedure is used to tackle the problem of not having a sky region that is commonly covered by all maps. The final number of principal components in the model is three and maps can be generated within a total range from 10 to 408 MHz. Same as for GSM no individual treatment of point-like sources is mentioned.

As a measure of accuracy, the relative difference between the LWA1 survey at 74 MHz and the model prediction at the same frequency was calculated. Deviations were found to be at an overall level of 10 %.

The LWA1 surveys nicely cover the low-radio regime < 100 MHz. However, the Long Wavelength Array is stationed in the northern hemisphere. This could lead to additional uncertainties in the interpolated maps at Galactic latitudes below -40° , which would become relevant for experiments in the southern hemisphere. Furthermore, the temperature scale of the LFSM output strongly depends on the calibration of the LWA1 surveys, as these represent a large fraction of the total ensemble of input maps. Potential systematic errors in the calibration would thus directly bias the interpolation model.

2.5. Other parametrizations of the Galactic background brightness

Besides the interpolation models for generating all-sky maps, there are also some parametrizations for the spectrum of the average brightness of the Galactic background. We do not include them in the comparison of the interpolation models but present and show them here for completeness.

One of these parametrizations was introduced by Cane (1979) and assumes a superposition of Galactic and extragalactic contributions to the brightness including absorption by the Galactic disk and was fitted to a multitude of measurements of the polar regions of the Galaxy. This yields lower brightness temperatures than expected for an average of the whole sky because the bright Galactic center is not considered here. To accommodate for this, a correction factor of ~ 1.3 to the Galactic brightness contribution was found by Dulk et al. (2001) and Durc et al. (2003). In this work, we use the such-corrected parametrization and refer to it as "Cane".

The parametrization by Cane was revisited again by Tokarsky, Konovalenko and Yerin (Tokarsky et al. 2017), where the corrections were summarized and another expression for the average brightness temperature as a function of frequency was given based on results from Krymkin (1971). We refer to this parametrization here as "TKY".

Both descriptions of the Galactic background brightness are applicable only for the low-frequency radio regime (< 100 MHz), where the Galaxy is the dominant contribution to the background.

Furthermore for comparison purposes, we show the simple approach of scaling a full-sky map with just one single spec-

Table 1: Summary of all presented reference maps with their sky coverage and quoted uncertainties.

Map No.	Frequency ν (MHz)	Covered Declination	σ_k (%)	σ_{T_0} (K)	σ_{T_0} (Normalized) (%)	Used In	References
1	10	$-6^\circ < \delta < 74^\circ$	9*	$2 \cdot 10^4$	7.0	1,2,3	1
2	22	$-28^\circ < \delta < 80^\circ$	16	$5 \cdot 10^3$	11.5	1,2,3,4	2
3	40	$-40^\circ < \delta < 90^\circ$	20	10	0.1	3	3
4	45	$-90^\circ < \delta < 65^\circ$	10/15	125^\dagger	1.5	1,2,3,(4)	4, 5
5	50	$-40^\circ < \delta < 90^\circ$	20	10	0.2	3	3
6	60	$-40^\circ < \delta < 90^\circ$	20	10	0.2	3	3
7	70	$-40^\circ < \delta < 90^\circ$	20	10	0.3	3	3
8	80	$-40^\circ < \delta < 90^\circ$	20	10	0.5	3	3
9	85	$-25^\circ < \delta < 25^\circ$	7	120	6.7	2	6
10	150	$-25^\circ < \delta < 25^\circ$	5	40	9.2	2	6
11	178	$-5^\circ < \delta < 88^\circ$	10	15	5.3	(1,2,3)	7
12.a	408	$-90^\circ < \delta < 90^\circ$	10/5	3	8.8	1	8
12.b	408	$-90^\circ < \delta < 90^\circ$	10/5	3	8.8	4	9
12.c	408	$-90^\circ < \delta < 90^\circ$	10/5	3	8.8	2,3	10

Notes. The two values for the relative scale uncertainty of map No. 4 refer to the two different estimations for this in the publications of the northern and southern part of the survey, respectively. For scale uncertainties with a (*) no explicit value was given by the authors. Instead, we estimate it by taking half of the smallest contour interval of that map and dividing it by its minimum brightness temperature. In the same way, zero-level errors with a (\dagger) are estimated by taking half of the smallest contour interval. To give the zero-level errors as a fraction of the average sky temperature, we calculate the latter from Eq. 4, where we take the average from using all four considered sky models. For indicating in which models the maps are used, we use the following notation: 1 = GSM, 2 = GSM16, 3 = LFSS, 4 = LFmap. Numbers in parentheses mark that the map was only used indirectly in the respective model.

References. (1) Caswell (1976); (2) Roger, R. S. et al. (1999); (3) Dowell et al. (2017); (4) Alvarez, H. et al. (1997); (5) Maeda, K. et al. (1999); (6) Landecker & Wielebinski (1970); (7) Turtle & Baldwin (1962); (8) Haslam et al. (1982); (9) Platania et al. (2003); (10) Remazeilles et al. (2015).

tral index. As the reference map, we use the 408 MHz map by Haslam et al. (1982) as improved by Remazeilles et al. (2015), which we introduce in Sect. 3. Here, we refer to this description as "Haslam", but also do not include it in the comparison of the interpolation models because of its drawbacks. Using a single spectral index does not represent reality, as the spectral index varies for different regions of the sky and different frequency regimes (Mozdzen et al. 2018; Dickinson et al. 2019). Although often used in studies of fast radio bursts, the Haslam description should not be seen as equivalent to the more sophisticated interpolation models (Price 2021). We show the Haslam results for a spectral index between -2.62 and -2.46 .

3. Reference maps

The presented radio sky interpolation models rely on a number of reference maps. Consequently, the accuracy of the models is dependent on the accuracy of these maps and their inherited uncertainties. Therefore, in the following, we give an overview of the reference maps used in the considered interpolation models.

10 MHz (Caswell 1976): This map by Caswell was obtained using the 10-MHz array at the Dominion Radio Astrophysical Radio Observatory (DRAO) in Canada. The observations were done during winter nights to minimize ionospheric influence. Thus the sky coverage is limited in right ascension from 0^{h} to 16^{h} . Relative calibration of the received signal strength to sky brightness temperature was performed by comparing the observations to a published 178 MHz map from Turtle & Baldwin (1962), that was scaled using a power-law relation as in Eq. 2 and spectral indices of -2.40 and -2.75 for the Galactic and extragalactic isotropic emission, respectively. The sky brightness is

mapped in contours indicating specific temperature levels. The contour interval between these levels is $2 \cdot 10^4$ K.

22 MHz (Roger, R. S. et al. 1999): The sky map at 22 MHz was also produced from measurements done at the DRAO. The applied antenna gain is based on an assumed value for the flux density of Cygnus A (Roger et al. 1969). A cross-check of the map with the 408 MHz map by Haslam et al. (1982) was performed to compare the temperature scales by producing scatter plots of the brightness temperatures (T - T plots) from both maps for different declinations from the zenith. Then, the temperature scale of the 22 MHz map was tuned to overall match the ratio at the zenith, for which the authors believed their instrument to be understood better. The T - T plot for the zenith direction showed no discrepancy with the zero-level of the temperature scale. Also, the differential spectral index derived from the T - T plot between the 22 MHz map and the 408 MHz map is in agreement with other measurements.

LFSS 40 MHz, 50 MHz, 60 MHz, 70 MHz, 80 MHz (Dowell et al. 2017): Within the LFSS at the LWA1, sky maps were produced at a variety of frequencies. The gain of the LWA1 antennas was derived from an electromagnetic antenna model in combination with a correction using bright pulsars at different elevations as reference sources. Previous observations of the flux density of Cygnus A by Baars et al. (1977) were used to convert the measurements into sky temperature. A temperature calibration system was used to achieve absolute accuracy of 10 K or better.

45 MHz (Alvarez, H. et al. 1997; Maeda, K. et al. 1999): At 45 MHz, there are two separate sky surveys available, one covering the northern hemisphere and one covering the southern hemi-

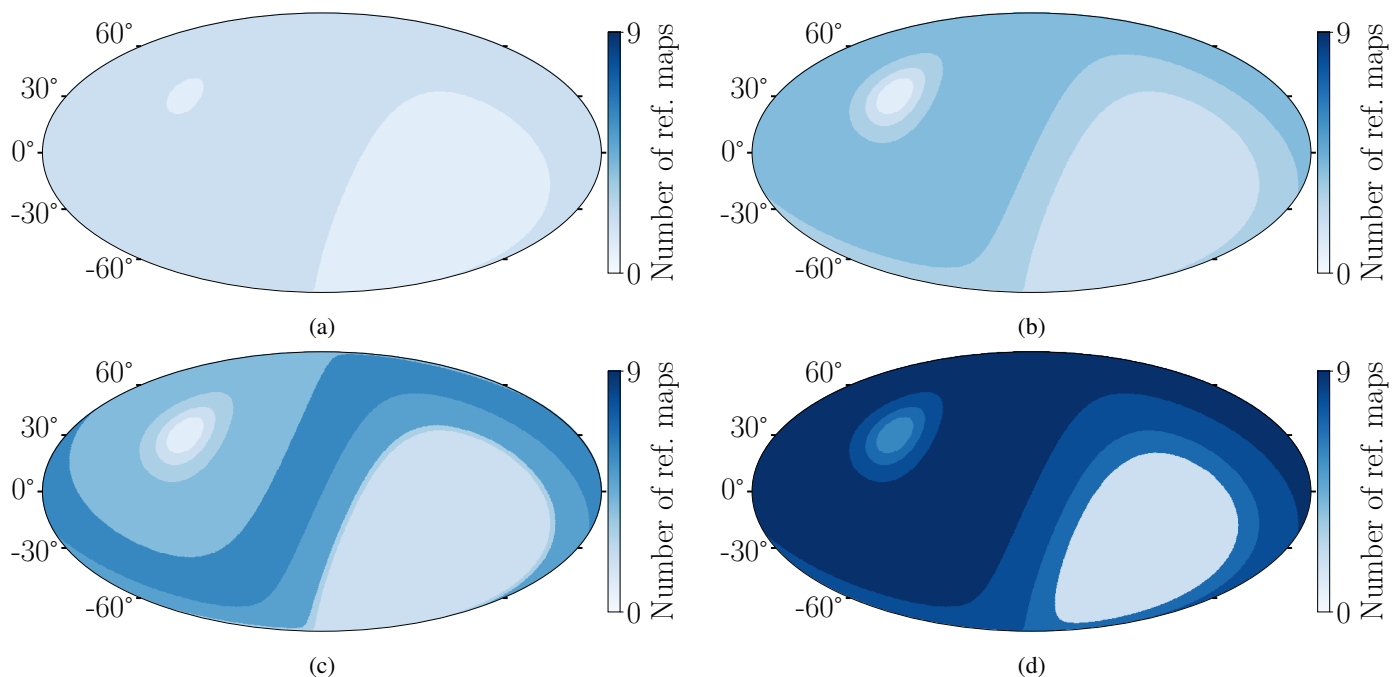


Fig. 1: Sky coverages of the used reference maps for each sky model laid on top of each other and plotted in galactic coordinates. The models are numbered (a) LFmap, (b) GSM, (c) GSM16 and (d) LFSM. For regions of lighter color fewer measurements from reference maps are available than for regions of darker color.

sphere conducted at the Middle and Upper Atmosphere Radar in Japan and the Maipu Radio Astronomy Observatory in Chile, respectively. Calibration of the temperature scale of the latter survey was performed by using a spectral interpolation from data in a well-observed reference region and comparison with the measurements. The map was later used to calibrate the map of the northern hemisphere as both cover the region from 5° to 19° in declination.

85 MHz, 150 MHz (Landecker & Wielebinski 1970): Surveys at 85 MHz and 150 MHz were made using the Parkes 64 m telescope in Australia. Calibration of the temperature scale was done after every scan with well-matched noise diodes that could be connected to the receivers of the telescope.

408 MHz (Haslam et al. 1982): Multiple sites (Jodrell Bank MkI(A) telescope in England, Effelsberg 100 m telescope in Germany and Parkes 64 m telescope in Australia) were used to observe the sky at 408 MHz. The originally assembled map by Haslam et al. was calibrated with reference to a sky survey at 404 MHz from Pauliny-Toth & Shakeshaft (1962). (Remazeilles et al. 2015) believe that the brightness temperature scale is more accurate ($\sim 5\%$) than originally quoted ($\sim 10\%$). Because of its importance in the field of radio astronomy, the map and its raw data were restudied multiple times, including destriping it and removing point-like sources (Platania et al. 2003; Remazeilles et al. 2015).

Corrections to the maps at 45 MHz, 150 MHz and 408 MHz: The sky surveys at 45 MHz that are used in the interpolation models considered here were done separately for the southern (Alvarez, H. et al. 1997) and northern hemisphere (Maeda, K. et al. 1999). In a later study, the maps were combined into an

all-sky survey with a correction of the zero-level of -544 K (Guzmán et al. 2011) to the combined map. This corresponds to $\sim 6.5\%$ of the average sky temperature at that frequency and is more than three times larger than the originally quoted error on the zero-level. In the same study also a zero-level correction for the original 408 MHz map of -3.46 K was determined, which corresponds to $\sim 10\%$ of the average sky temperature.

Another recalibration was performed for the combined 45 MHz map (although without the mentioned zero-level correction) and for the 150 MHz map (Monsalve et al. 2021). There the maps were corrected for temperature scale and zero-level to best match data taken with the Experiment to Detect the Global EoR Signature (EDGES) (Bowman et al. 2018). Scale correction factors are 1.076 ± 0.017 and 1.112 ± 0.012 for the sky temperature of the 45 MHz and 150 MHz maps, respectively. Zero-level corrections for the surveys are -160 ± 78 K and 0.7 ± 6.0 K, which correspond to $1.9 \pm 0.9\%$ and $0.2 \pm 1.4\%$ of the average sky temperature at the respective frequencies.

Corrections to the temperature scale and zero-level by matching to other, sometimes newer data can be bigger than originally quoted uncertainties. This hints towards an underestimation of the latter and poses a challenge when trying to place trust on individual surveys.

Summary: The reference maps are listed in Table 1 together with their quoted uncertainties on the temperature scale, which are typically described by a linear relation. The true temperature T_{true} relates to the observed temperature T_{obs} as

$$T_{\text{true}} = k \cdot T_{\text{obs}} + T_0. \quad (3)$$

The scaling factor k ideally has a value of 1, but it inherits the relative scale uncertainty σ_k , which goes up to 20% for the reference maps presented here, while the largest uncertainties are

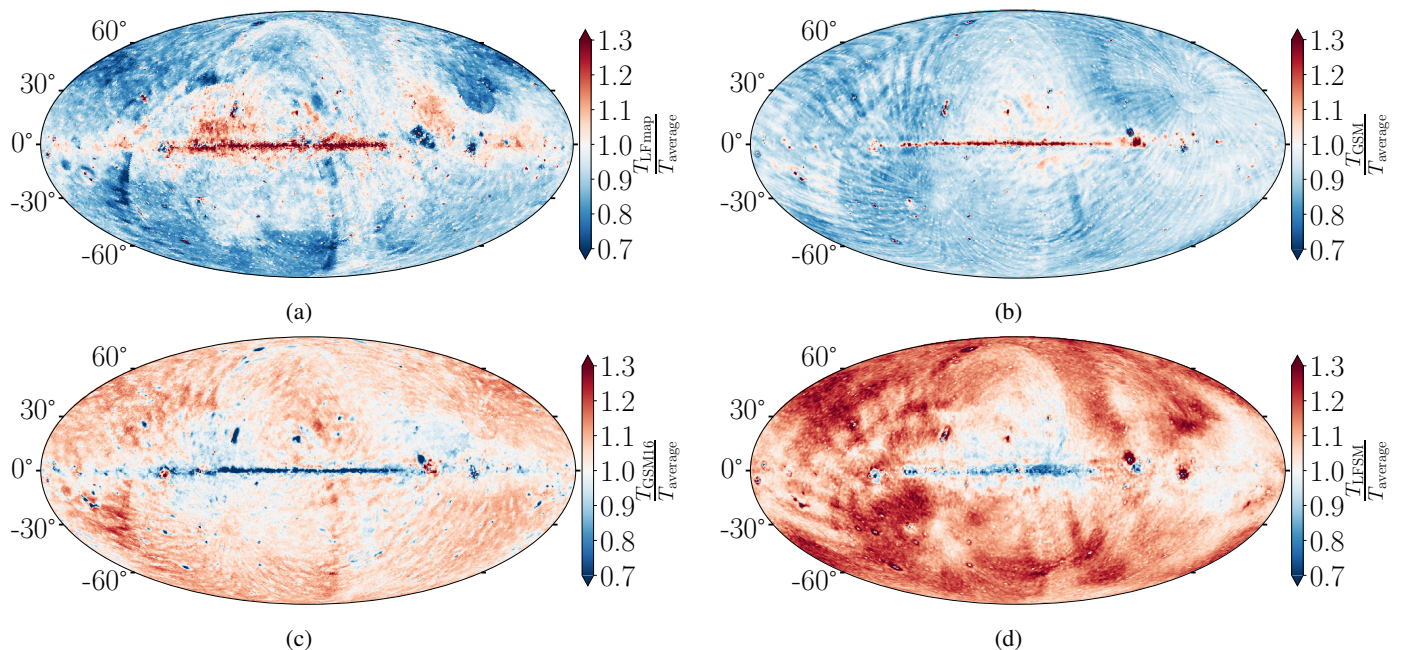


Fig. 2: Sky maps showing the temperature ratio of each model to the average from all four models at 50 MHz. The models are denoted as (a) LFmap, (b) GSM, (c) GSM16 and (d) LFSM.

quoted for the results of the Low Frequency Sky Survey (LFSS) (map No. 3, 5 to 8). The zero-level T_0 represents an absolute offset of the temperature scale and deviations from the ideal case ($T_0 = 0$ K) are reflected in the zero-level error σ_{T_0} . The zero-level errors of the reference maps are given in Table 1 as absolute values and also relative to the average brightness temperature of the whole sky at the respective frequency, where the average sky brightness temperature is calculated as in Eq. 4. The relative zero-level errors amount up to $\sim 12\%$, while they are negligible for the LFSS results.

Furthermore, Table 1 gives the information, in which models each reference map is used. This information is also visualized in Fig. 1, where for each model the covered sky regions of all used reference maps are superimposed. LFmap relies on only two reference maps with the approach of spectral scaling. LFSM uses the most reference maps with a maximum of nine maps covering the region between -6° and 65° of declination. However, there is a lack of available reference maps for all models around the south celestial pole.

Further maps at higher frequencies are used in the interpolation models as well. Many of them were generated from data taken with the space-based instruments Wilkinson Microwave Anisotropy Probe (WMAP) and Planck (Hinshaw et al. 2009; Planck Collaboration et al. 2016). These maps are important for modeling sky regions where fewer low-frequency surveys were performed, but they will not be discussed in more detail here.

4. Comparison of the sky model predictions

Besides the quoted accuracies of the reference maps, which propagate into the interpolation models, we compare the output of the models directly. We study the deviations between them and determine their level of agreement, which we then use as an estimator for the systematic uncertainty in predicting the diffuse Galactic radio emission on an absolute scale.

The PyGDSM (Price 2016) package is used as an interface to the GSM, GSM16 and LFSM models. It employs the healpy

(Zonca et al. 2019) package to provide the temperature map output of the models in the HEALPix (Górski et al. 2005) format. LFmap is a C program and is available at the author's website¹. After generating the LFmap output maps we convert them as well into the HEALPix format. Exemplarily, sky maps are shown in Fig. 2, which display the temperature ratio between the output of each model and the average at 50 MHz. The average is calculated pixelwise from all four models at the same frequency. At 50 MHz LFmap and GSM predict a hotter Galactic center than the other two models, while away from the center their predictions are colder. By this depiction, also spatial structures of the differences between the models are visible, e.g. some stripe-like features for GSM.

In this study, the comparison is conducted for the frequency range from 30 to 408 MHz. Typically radio arrays for the detection of cosmic particles are not operated below 30 MHz because of the presence of strong atmospheric noise (Huege 2016; Union 2019). The upper bound arises from limitations within the LFmap and LFSM models.

4.1. Comparison of the total sky

The average temperature of the sky at a given frequency ν is calculated as

$$T_{\text{sky, average}}(\nu) = \frac{1}{4\pi} \int_{-\pi}^{\pi} dl \int_{-\frac{\pi}{2}}^{\frac{\pi}{2}} db \cos(b) T(\nu; l, b), \quad (4)$$

where l is the Galactic longitude and b is the Galactic latitude. The brightness temperature at a specific location in the sky $T(\nu; l, b)$ is taken from maps in Galactic coordinates produced with the sky models. The observable $T_{\text{sky, average}}(\nu)$ is used for the first part of the comparison. It gives compressed information of a sky map while ignoring spatial structures. For the Galactic

¹ <https://www.astro.umd.edu/~emilp/LFmap/>

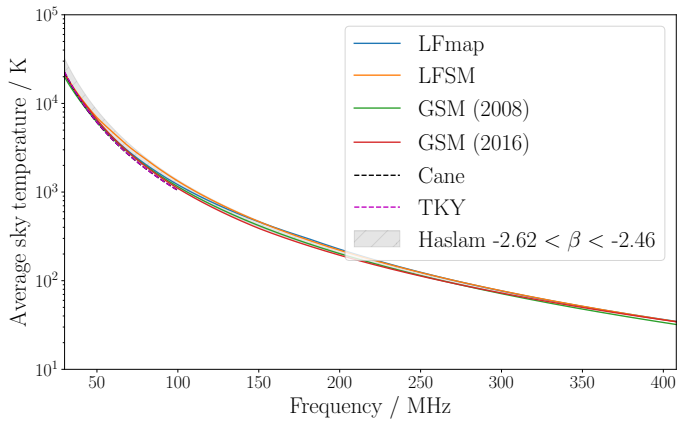


Fig. 3: Average sky temperature as a function of the frequency is plotted for the four interpolation models as solid lines and for the parameterizations Cane and TKY as dashed lines. The grey band shows the results for the 408 MHz Haslam map when scaled down with a spectral index β between -2.62 and -2.46 .

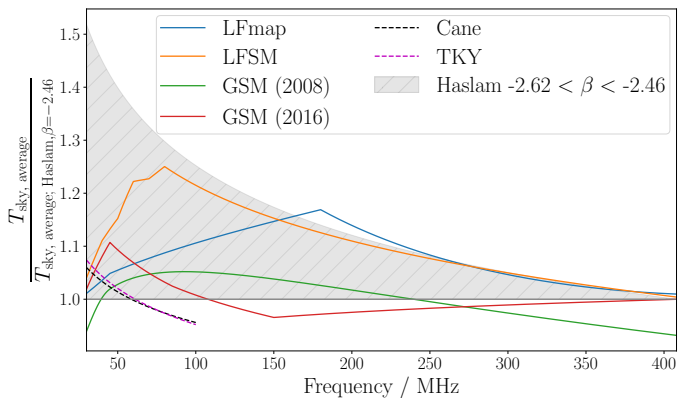


Fig. 4: Average sky temperature is plotted against the frequency as in Fig. 3 with the same line style, but normalized to the results for the scaled Haslam map and a spectral index $\beta = -2.46$.

Calibration of an antenna without a narrow beam, taking into account fine spatial structures is not as relevant, because the measured quantity of received power is a folding of the whole visible sky through the antenna pattern.

Figure 3 shows the average sky temperature as a function of the frequency for the interpolation models from 30 MHz to 408 MHz. The grey band is obtained from the Haslam description of the sky brightness by using a spectral index β between -2.62 and -2.46 and is shown for comparison. The range for the spectral index is deduced from recent measurements (Mozdzen et al. 2016, 2018) around the relevant frequencies.

Furthermore, the previously introduced parametrizations of the average sky brightness below 100 MHz, Cane and TKY are shown for comparison as solid and dashed black lines, respectively.

The comparison shows that the interpolation models agree well in their shapes over the whole frequency range, while they are systematically shifted relative to each other. This can be seen more quantitatively in Fig. 4, in which the data are normalized to the Haslam results with a spectral index $\beta = -2.46$, to better show spectral behaviour of the models.

Next, we calculate the relative difference of the average sky temperatures at a given frequency for any combination of mod-

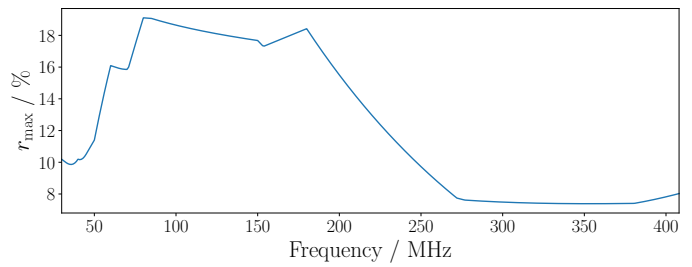


Fig. 5: Maximum relative difference of the average sky temperature between any two of the considered models as a function of frequency. The maximum relative difference is calculated as in Eq. 5.

Table 2: Value of r_{m_1, m_2} listed for each combination of the interpolation models.

r_{m_1, m_2} (%)	LFmap	GSM	GSM16	LFSM
LFmap	-	4.6	0.7	-7.3
GSM	-4.6	-	-3.8	-11.9
GSM16	-0.7	3.8	-	-8.1
LFSM	7.3	11.9	8.1	-

Notes. The header row gives the model m_1 and the leftmost column gives the model m_2 . Positive values show that the model m_1 produces maps with higher average temperatures than the model m_2 .

els m_1 and m_2 . From that, we evaluate the maximum relative difference

$$r_{\max}(\nu) = \max \left| 2 \cdot \frac{T_{\text{sky, average}, m_1}(\nu) - T_{\text{sky, average}, m_2}(\nu)}{T_{\text{sky, average}, m_1}(\nu) + T_{\text{sky, average}, m_2}(\nu)} \right|, \quad (5)$$

which we plot as a function of the frequency, shown in Fig. 5. The maximum relative difference noticeably rises for frequencies larger than ~ 50 MHz to values around 18 % and drops again for frequencies larger than ~ 200 MHz to values around 8 %.

To gauge the level of agreement between the models more concisely, for each of them we integrate the average sky temperature over the frequency range from 30 to 408 MHz, and calculate a relative difference r_{m_1, m_2} pairwise as

$$r_{m_1, m_2} = 2 \cdot \frac{\int_{30\text{MHz}}^{408\text{MHz}} T_{\text{sky, average}; m_1}(\nu) - T_{\text{sky, average}; m_2}(\nu) d\nu}{\int_{30\text{MHz}}^{408\text{MHz}} T_{\text{sky, average}; m_1}(\nu) + T_{\text{sky, average}; m_2}(\nu) d\nu}, \quad (6)$$

again with any combination of models m_1 and m_2 . The results are listed in Table 2. By this comparison, all models agree with each other at a level of around 12% or better. Here, the LFSM prediction shows the largest deviation relative to the other models. The level of agreement is 5% when neglecting the LFSM. This could be a consequence of the latter containing the five LWA1 maps of the northern hemisphere between 30 and 80 MHz, which have a significant influence on the principal component analysis. The other interpolation models have fewer reference maps in that frequency range and this regime might thus be influenced more by the included GHz maps.

4.2. Comparison of the local sky

The differences between the models are not just reflected in general deviations of the temperature scales. They also show structural variations that become noticeable by comparing specific

sky regions, e.g. on/off the Galactic plane. These variations influence the model comparison when confining their output maps to the sky coverage of a specific radio-detection experiment on Earth. The local sky of an observer changes with the local sidereal time (LST) and solely depends on the observer's geographic latitude if the experiment is operated both day and night.

The average temperature of a local sky is obtained by converting a map into the horizontal coordinate system with the two angles azimuth α and altitude a (the elevation angle above horizontal), thus limiting it to the visible half of the sky above the horizon and integrating over this region. The results are then averaged for varying LST from 0 h to 24 h as

$$T_{\text{local sky, average}}(\nu, l) = \frac{1}{2\pi} \int_{0\text{h}}^{24\text{h}} dt_{\text{LST}} \int_0^\pi da \int_{-\frac{\pi}{2}}^{\frac{\pi}{2}} d\alpha \cos(a) T(\nu, l, t_{\text{LST}}; a, \alpha) \quad (7)$$

for a given latitude l of the observer on Earth. We further integrate the average temperature of the local sky over frequency:

$$\Sigma T(l) = \int_{30\text{MHz}}^{408\text{MHz}} T_{\text{local sky, average}}(\nu, l) d\nu \quad (8)$$

The result of this integral is plotted for each interpolation model as a function of the observer's latitude in Fig. 6 a). It is clear that ΣT changes depending on the exposure to the radio-bright center of the Galaxy. At the northern celestial pole (90° latitude) this exposure is the smallest and thus ΣT is the lowest over all frequencies, while the maximum exposure takes place at around -60° of latitude.

Furthermore, differences between the interpolation models are recognizable. Apart from a general shift in the temperature scale there are latitude dependent variations, which are probably due to different ratios in the models between the coldest and hottest regions of the sky.

Figure 6 b) shows the same results as in Fig. 6 a), but normalized to those of the GSM2008 model, which on average gives the coldest sky maps. Here the level of agreement is found to be 15% in the worst case, when comparing to the LFSM results. The latter model shows the largest deviation with respect to the other ones in the same way as evident from the comparison in Table 2. The level of agreement between the three remaining models for all observer latitudes is better than 7%.

5. Comparison for selected radio experiments

The comparison of the sky models based on the local sky is further carried out for selected radio arrays for the detection of cosmic particles, namely RNO-G (surface antennas) (Aguilar et al. 2021), LOFAR (Schellart, P. et al. 2013), GRAND (Álvarez-Muñiz et al. 2020), SKA-low (Buitink et al. 2021), the Pierre Auger Observatory (AERA (Huege, T., Aab, A., Abreu, P., et al. 2019) and the AugerPrime Radio Detector (Pont 2019)) and the radio antennas of the IceCube surface array (Abbasi et al. 2021). The sky models compare differently for each of the experiments. This is due to them being situated at different geographical latitudes and using different frequency bands. For this study, we make the simplifying assumption of a constant antenna sensitivity over the whole frequency band for all arrays. Also, we further restrict the local sky seen by the antennas to altitude angles between 15° and 90° above the horizon to simulate a uniform gain pattern in that range.

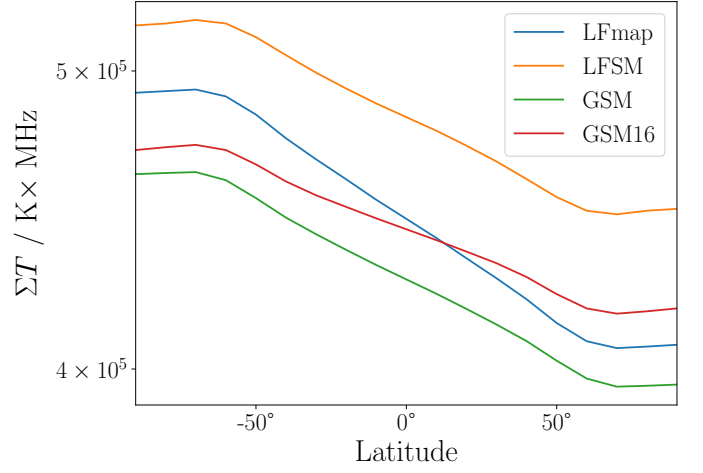


Fig. 6: Values of $\Sigma T(l)$ for each sky interpolation models as a function of latitude.

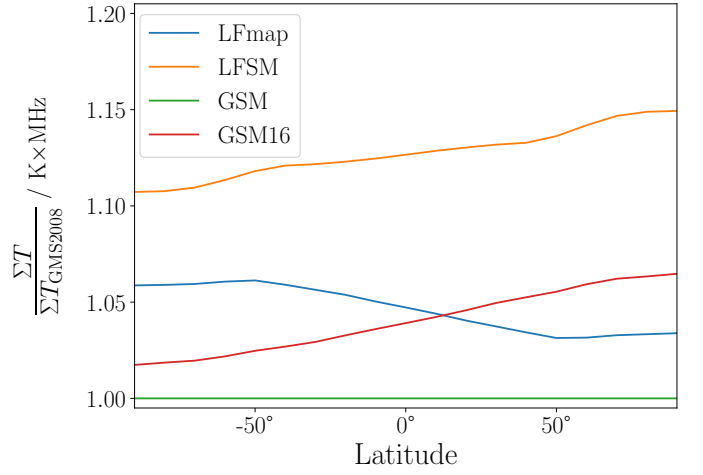


Fig. 7: Values of $\Sigma T(l)$ for each sky interpolation models, same as in Fig. 6 but normalized to the GSM curve.

Subsequently, the average temperature of the local sky integrated over LST is calculated analogous to Eq. 8 as

$$\Sigma T(l_{\text{Exp}}) = \int_{\nu_{\text{Exp, lower}}}^{\nu_{\text{Exp, upper}}} T_{\text{local sky, } 15^\circ \text{ to } 90^\circ, \text{ average}}(\nu, l_{\text{Exp}}) d\nu, \quad (9)$$

in which the frequency band ($\nu_{\text{Exp, lower}}$, $\nu_{\text{Exp, upper}}$) and the latitude (l_{Exp}) are adapted to the respective experiment. Further, any two sky models m_1 and m_2 are compared by their relative difference

$$r_{\text{Exp; } m_1, m_2} = 2 \cdot \frac{\Sigma T_{m_1}(l_{\text{Exp}}) - \Sigma T_{m_2}(l_{\text{Exp}})}{\Sigma T_{m_1}(l_{\text{Exp}}) + \Sigma T_{m_2}(l_{\text{Exp}})}. \quad (10)$$

The largest relative differences obtained for each experiment are listed in Table 3 together with the properties of the experiment and the combination of sky models between which the largest relative difference occurs. These differences range from $\sim 10\%$ to $\sim 19\%$. When excluding LFSM, the differences are smaller than 10% for all experiments except for IceCube and the high band of LOFAR with a difference of $\sim 13\%$ between the LFmap and GSM16 models.

An extended overview of the comparison results for each of the experiments is given in appendix A.

6. Influence of radio emission from the quiet Sun

Another source of radio background in the sky is the Sun. Here we study the influence of the quiet Sun on the average sky brightness, which describes the continuous thermal emission of solar radiation. There is also a concept of the active Sun, which includes enhanced emission during sunspot activity as well as emission in the context of solar flares. These contributions take place on limited timescales from seconds to hours and may significantly increase the received power in an antenna (Kraus 1986), but we do not cover them in this study.

Radio emission of the quiet Sun at frequencies from tens of MHz to tens of GHz is larger than expected from a 6000 K black body spectrum and reaches brightness temperatures up to 10^6 K around 50 MHz (Kraus 1986). To investigate how large the influence of the Sun is, we generate sky maps with a disc of constant brightness projected onto it. The disc matches the apparent size of the Sun. Data on the brightness temperature of the quiet Sun as a function of the frequency are taken from a summary of recent measurements given in (Zhang et al. 2022).

With the superimposed quiet Sun the average sky temperature of the map is calculated as before and its relative difference to the average sky temperature of the unmodified map is determined. This is shown for each of the four sky interpolation models in Fig. 8. While the influence is negligible at the lowest frequencies it grows to a level of $\sim 8\%$ at 400 MHz.

Furthermore, we adapt this procedure to the local skies of the selected radio arrays, again restricting them to elevations from 15° to 90° above the horizon and taking the mean of the average sky temperatures over the course of 24 h of LST. The relative difference caused by the Sun is shown for all arrays over their frequency bands in Fig. 9. The arrays at the lowest frequencies are shown on the left and the ones reaching to larger frequencies are shown on the right.

Analogue to Fig. 8 the relative differences increase with frequency, while they are scaled up here because only a portion of the total sky is considered. The differences are on the sub-percent level for Auger and the low band of LOFAR and go up to 20% for RNO-G at around 400 MHz. Deviations between the arrays at the same frequencies are attributable to the different exposure to the Galactic center due to their geographical positions.

7. Discussion

This study gives estimates for the systematic uncertainty in predicting the diffuse Galactic radio emission in the 30 to 408 MHz range. Moreover, it provides an overview of the available models that are used for making these predictions and their corresponding reference measurements. A considerable realization from this overview is that probably a significant level of correlation exists between the systematic uncertainties of the sky models and the reference maps. Some reference maps served as calibrators for other maps and have thus an increased weight in the sky interpolation models. In general, for the sky models considered here, there is no substantial attention paid to weighting the individual reference maps during the modeling process, which can lead to biases on the absolute temperature scale. These biases are almost impossible to untangle.

The generally small number of reference maps in the studied frequency range further complicates the situation. While many

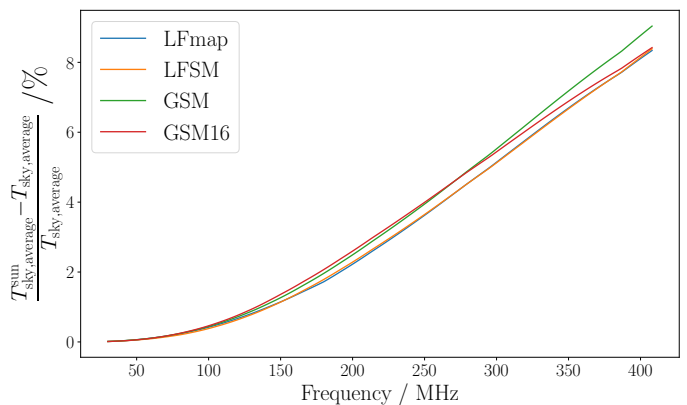


Fig. 8: Influence of the Sun on the average sky temperature for each of the models. The plot shows the relative difference of the average sky temperature as a function of the frequency for when a Sun sized circle of the corresponding brightness temperature (quiet Sun) is added to the maps.

surveys include a careful treatment of their uncertainties, others lack this kind of thoroughness, which in some cases may just be a consequence of the age of these surveys and the unavailability of some tools and techniques at the time of their execution.

In the future, these difficulties can be coped with by including more and newer reference maps into the sky interpolation models and weighting them based on their inherited uncertainties. New sky surveys at MHz frequencies are on the horizon or were recently published, including direct comparisons to other maps or sky models (Eastwood et al. 2018; Kriele et al. 2022).

Regarding the application of the Galactic Calibration for radio arrays in astroparticle physics, we argue that the viability of this method is given if systematic uncertainties are carefully taken care of, which means that the parameters of the considered radio array are important. From our studies, we see that the Galactic Calibration exhibits larger uncertainties at higher frequencies. There, the Galaxy's contribution to the radio background diminishes and sources like the Sun become stronger. In the case of an array with a large frequency band, it might be a solution to conduct the Galactic Calibration only with night-time measurements to minimize systematic uncertainties.

8. Conclusion

We compare four interpolation models that produce full-sky maps of the Galactic radio emission at frequencies between 30 and 408 MHz. The models partially rely on the same reference measurements and differ to a greater or lesser extent by their interpolation approach. A summary of the used reference maps shows relative uncertainties on the temperature scales of up to 20% and zero-level errors that can be as large as up to $\sim 12\%$ of the average temperature of the sky at that frequency. In a global comparison, we find that the predictions of the interpolation models all agree within $\sim 12\%$, which we suggest as an estimate for the systematic uncertainty of the model predictions. However, we would like to stress that LFSM stands out in this comparison and the other three models agree significantly better. This estimate for the systematic uncertainty of the model prediction incorporates both the individual temperature scale uncertainties of the reference maps and uncertainties because of different modeling methods.

Table 3: For each of the selected radio experiments the largest relative deviation $\max(r_{\text{Exp}; m_1, m_2})$ between any two sky models m_1 and m_2 is tabulated, while either including or excluding LFSM.

Experiment	l_{Exp} ($^\circ$)	Frequency Band (MHz)	$\max(r_{\text{Exp}; m_1, m_2})$ (%)	Corresponding Sky Models	$\max(r_{\text{Exp}; m_1, m_2})$ (Excl. LFSM) (%)	Corresponding Sky Models
RNO-G (1)	72.58	100 to 408	17.1	LFSM / GSM16	9.6	LFmap / GSM16
LOFAR low (2)	52.91	30 to 80	13.3	LFSM / GSM	8.9	GSM / GSM16
LOFAR high (3)	52.91	110 to 190	18.4	LFSM / GSM16	12.8	LFmap / GSM16
GRAND (4)	42.93	50 to 200	16.3	LFSM / GSM	2.0	LFmap / GSM
SKA-low (5)	-26.70	50 to 350	13.6	LFSM / GSM16	7.5	LFmap / GSM16
Auger (6)	-35.21	30 to 80	10.5	LFSM / GSM	4.8	LFmap / GSM
IceCube (7)	-90.0	70 to 350	18.6	LFSM / GSM16	13.6	LFmap / GSM16

Notes. Site locations and frequency bands of the experiments are quoted from latest design plans. For RNO-G the LPDA surface antennas are considered, which are sensitive up to ~ 1 GHz, but the comparison is done only up to 408 MHz because of the limitations of the LFmap and LFSM sky models. The complete table can be found in appendix A.

References. (1) Aguilar et al. (2021); (2) Schellart, P. et al. (2013); (3) Nelles et al. (2015); (4) Álvarez-Muñiz et al. (2020); (5) Buitink et al. (2021); (6) De Jong (2021); (7) Abbasi et al. (2021).

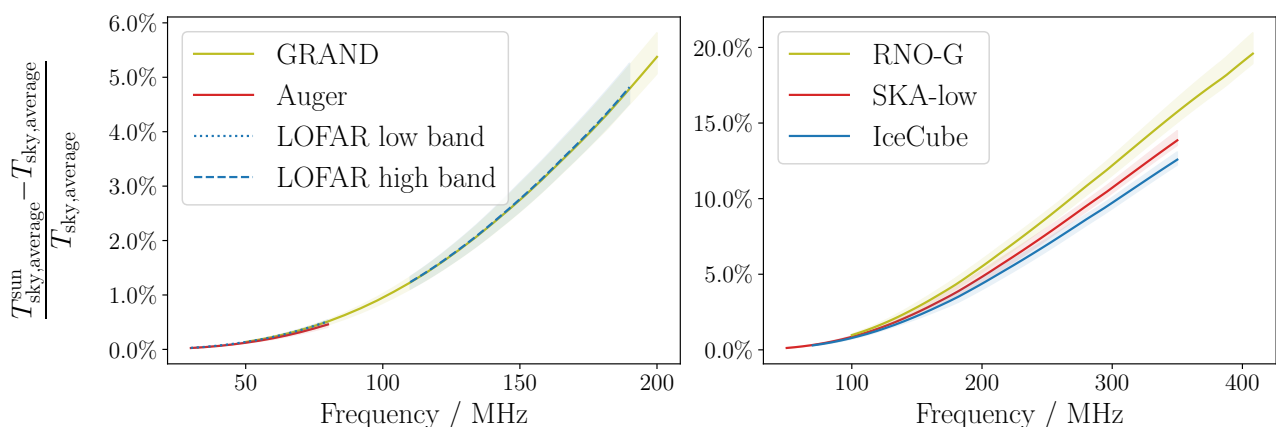


Fig. 9: Relative difference of the average temperature of the local sky induced by the quiet Sun for the selected radio arrays. The lines represent the average results from using the four sky models to produce the maps, while the maximum and minimum contribution from any model is shown by the colored bands. Arrays at lower frequencies are shown in the left part, while arrays at higher frequencies are shown on the right.

Furthermore, we compare the models based on the local sky at a given experiment’s latitude on Earth. This step reveals further differences between the models and in combination with specific frequency bands of selected radio-detection arrays deviations vary considerably. Depending on the experiment, the level of agreement lies between 10 % and 19 %. Again, these numbers decrease notably when excluding LFSM.

Additionally, we study the influence of the quiet Sun on the radio background of the selected arrays and find it to be negligible at lower frequencies. However, the contribution increases to ~ 20 % at around 400 MHz.

The relative uncertainties in sky temperature quoted above determine the signal power measured in radio detection arrays for cosmic particles – whereas the energy scale for the energy of the detected particles scales with the electric field amplitudes, i.e., the square root of the signal power. The relevant systematic uncertainty on the energy scale of particle detection thus corresponds to approximately half of the values quoted here. These uncertainties are typically competitive with those achieved with external calibration sources – if not better – and thus confirm the value of the Galactic Calibration approach. If models with even higher accuracy for the Galactic emission in the frequency band from 30 to 408 MHz become available in the future, ra-

dio detection arrays for cosmic particles will profit from these retroactively.

Acknowledgements.

References

- Aab, A., Abreu, P., Aglietta, M., et al. 2017, JINST, 12, T10005
Abbasi, R., Ackermann, M., Adams, J., et al. 2021, in Proceedings of 37th International Cosmic Ray Conference — PoS(ICRC2021), Vol. 395, 225
Aguilar, J., Allison, P., Beatty, J., et al. 2021, JINST, 16, P03025
Alvarez, H., Aparici, J., May, J., & Olmos, F. 1997, A&AS, 124, 315
Álvarez-Muñiz, J., Alves Batista, R., Balagopal V., A., et al. 2020, Sci. China Phys. Mech. Astron., 63, 219501
Baars, J. W. M., Genzel, R., Pauliny-Toth, I. I. K., & Witzel, A. 1977, A&A, 500, 135
Bowman, J. D., Rogers, A. E. E., Monsalve, R. A., Mozdzen, T. J., & Mahesh, N. 2018, Nature, 555, 67
Bridle, A. H. & Baldwin, J. E. 1967, MNRAS, 136, 219
Buitink, S., Corstanje, A., Falcke, H., et al. 2021, in Proceedings of 37th International Cosmic Ray Conference — PoS(ICRC2021), Vol. 395, 415
Cane, H. V. 1979, MNRAS, 189, 465
Caswell, J. L. 1976, MNRAS, 177, 601
De Jong, S. 2021, PoS, ICHEP2020, 829
de Oliveira-Costa, A., Tegmark, M., Gaensler, B. M., et al. 2008, MNRAS, 388, 247–260
Dickinson, C., Barr, A., Chiang, H. C., et al. 2019, MNRAS, 485, 2844

- Dowell, J., Taylor, G. B., Schinzel, F. K., Kassim, N. E., & Stovall, K. 2017, *MNRAS*, 469, 4537–4550
- Dulk, G. A., Erickson, W. C., Manning, R., & Bougeret, J. L. 2001, *A&A*, 365, 294
- Durc, N., Theodorou, A., Smith, K., et al. 2003, RFI Report for the US South-West, ftp://gemini.haystack.edu/pub/lofar/siting_docs/SWUS_RFI.doc, "accessed 23-August-2021"
- Eastwood, M. W., Anderson, M. M., Monroe, R. M., et al. 2018, *AJ*, 156, 32
- Ellingson, S. W., Taylor, G. B., Craig, J., et al. 2013, *IEEE Transactions on Antennas and Propagation*, 61, 2540
- Fodran, T., Abreu, P., Aglietta, M., et al. 2021, in *Proceedings of 37th International Cosmic Ray Conference — PoS(ICRC2021)*, Vol. 395, 270
- Górski, K. M., Hivon, E., Banday, A. J., et al. 2005, *ApJ*, 622, 759
- Guzmán, A. E., May, J., Alvarez, H., & Maeda, K. 2011, *A&A*, 525, A138
- Haslam, C. G. T., Salter, C. J., Stoffel, H., & Wilson, W. E. 1982, *A&AS*, 47, 1
- Hinshaw, G., Weiland, J. L., Hill, R. S., et al. 2009, *ApJS*, 180, 225
- Huege, T. 2016, *Phys. Rep.*, 620, 1
- Huege, T., Aab, A., Abreu, P., et al. 2019, in *EPJ Web of Conf.*, Vol. 210, 05011
- Kraus, J. D. 1986, *Radio Astronomy*, 2nd edn. (Cygnus-Quasar Books)
- Kriele, M. A., Wayth, R. B., Bentum, M. J., Juswardy, B., & Trott, C. M. 2022, *PASA*, 39, e017
- Krymkin, V. V. 1971, *Radiophys. & Quant. Electr.*, 14, 161
- Landecker, T. L. & Wielebinski, R. 1970, *Aust. J. Phys. Astrophys. Suppl.*, 16, 1
- Maeda, K., Alvarez, H., Aparici, J., May, J., & Reich, P. 1999, *A&AS*, 140, 145
- Monsalve, R. A., Rogers, A. E. E., Bowman, J. D., et al. 2021, *ApJ*, 908, 145
- Mozdzen, T. J., Bowman, J. D., Monsalve, R. A., & Rogers, A. E. E. 2016, *MNRAS*, 464, 4995
- Mozdzen, T. J., Mahesh, N., Monsalve, R. A., Rogers, A. E. E., & Bowman, J. D. 2018, *MNRAS*, 483, 4411
- Mulrey, K., Bonardi, A., Buitink, S., et al. 2019, *Astropart. Phys.*, 111
- Nelles, A., Schellart, P., Buitink, S., et al. 2015, *Astropart. Phys.*, 65, 11
- Pauliny-Toth, I. K. & Shakeshaft, J. R. 1962, *MNRAS*, 124, 61
- Planck Collaboration, Adam, R., Ade, P. A. R., et al. 2016, *A&A*, 594, A1
- Platania, P., Burigana, C., Maino, D., et al. 2003, *A&A*, 410
- Polisenky, E. 2007, *LFmap: A Low Frequency Sky Map Generating Program*, Tech. rep., Naval Research Laboratory
- Pont, B. 2019, *PoS, ICRC2019*, 395
- Price, D. C. 2016, *PyGSM: Python interface to the Global Sky Model*, *Astrophysics Source Code Library*, record ascl:1603.013
- Price, D. C. 2021, *Res. Notes AAS*, 5, 246
- Purton, C. R. 1966, *MNRAS*, 133, 463
- Reber, G. 1944, *ApJ*, 100, 279
- Remazeilles, M., Dickinson, C., Banday, A. J., Bigot-Sazy, M. A., & Ghosh, T. 2015, *MNRAS*, 451, 4311
- Roger, R. S., Costain, C. H., & Lacey, J. D. 1969, *AJ*, 74, 366
- Roger, R. S., Costain, C. H., Landecker, T. L., & Swerdlyk, C. M. 1999, *A&AS*, 137, 7
- Rogers, A. E. E. & Bowman, J. D. 2008, *AJ*, 136, 641
- Rybicki, G. B. & Lightman, A. P. 1985, *Radiative Processes in Astrophysics* (John Wiley & Sons, Ltd)
- Schellart, P., Nelles, A., Buitink, S., et al. 2013, *A&A*, 560, A98
- Schröder, F. G. 2017, *Progr. Part. Nucl. Phys.*, 93, 1
- Tokarsky, P. L., Konovalenko, A. A., & Yerin, S. N. 2017, *IEEE Transactions on Antennas and Propagation*, 65, 4636
- Turtle, A. J. & Baldwin, J. E. 1962, *MNRAS*, 124, 459
- Union, I. T. 2019, *Recommendation ITU-R P.372-14*, *Radio Noise*
- Webster, A. S. 1974, *MNRAS*, 166, 355
- Wilson, T. L., Rohlfis, K., & Hüttemeister, S. 2009, *Tools of Radio Astronomy* (Springer)
- Zhang, P., Zucca, P., Kozarev, K., et al. 2022, *ApJ*, 932, 17
- Zheng, H., Tegmark, M., Dillon, J. S., et al. 2016, *MNRAS*, 464, 3486–3497
- Zonca, A., Singer, L., Lenz, D., et al. 2019, *The Journal of Open Source Software*, 4, 1298

Appendix A: Complete model comparison for selected radio experiments

The results given in Table 3 are condensed to show the maximum deviation between any two models for all selected radio arrays. The full comparison for all models is given in Table A.1 in which the values of r_{m_1, m_2} are listed for all experiments and all combination of models m_1, m_2 .

Table A.1: Values of r_{m_1, m_2} for each combination of the interpolation models and for all selected radio arrays.

LOFAR low				
r_{m_1, m_2} (%)	LFmap	GSM	GSM16	LFSM
LFmap	-	3.5	-5.5	-9.8
GSM	-3.5	-	-8.9	-13.3
GSM16	5.5	8.9	-	-4.3
LFSM	9.8	13.3	4.3	-
LOFAR high				
r_{m_1, m_2} (%)	LFmap	GSM	GSM16	LFSM
LFmap	-	7.6	12.8	-5.6
GSM	-7.6	-	5.2	-13.2
GSM16	-12.8	-5.2	-	-18.4
LFSM	5.6	13.2	18.4	-
GRAND				
r_{m_1, m_2} (%)	LFmap	GSM	GSM16	LFSM
LFmap	-	2.0	1.5	-14.3
GSM	-2.0	-	-0.5	-16.3
GSM16	-1.5	0.5	-	-15.8
LFSM	14.3	16.3	15.8	-
SKA-low				
r_{m_1, m_2} (%)	LFmap	GSM	GSM16	LFSM
LFmap	-	5.2	7.5	-6.1
LFmap	-	5.2	7.5	-6.1
GSM16	-7.5	-2.3	-	-13.6
LFSM	6.1	11.3	13.6	-
Auger				
r_{m_1, m_2} (%)	LFmap	GSM	GSM16	LFSM
LFmap	-	4.8	0.7	-5.6
GSM	-4.8	-	-4.2	-10.5
GSM16	-0.7	4.2	-	-6.3
LFSM	5.6	10.5	6.3	-
IceCube				
r_{m_1, m_2} (%)	LFmap	GSM	GSM16	LFSM
LFmap	-	9.6	13.6	-5.0
GSM	-9.6	-	4.0	-14.6
GSM16	-13.6	-4.0	-	-18.6
LFSM	5.0	14.6	18.6	-
RNO-G				
r_{m_1, m_2} (%)	LFmap	GSM	GSM16	LFSM
LFmap	-	6.5	9.6	-7.6
GSM	-6.5	-	3.1	-14.0
GSM16	-9.6	-3.1	-	-17.1
LFSM	7.6	14.0	17.1	-